

Article

Role of Cr Element in Highly Dense Passivation of Fe-Based Amorphous Alloy

Ziqi Song ¹, Zhaoxuan Wang ¹, Qi Chen ¹, Zhigang Qi ¹, Ki Buem Kim ²  and Weimin Wang ^{1,*} 

¹ Key Laboratory for Liquid-Solid Structural Evolution and Processing of Materials (Ministry of Education), School of Materials Science and Engineering, Shandong University, Jinan 250061, China; 202234218@mail.sdu.edu.cn (Z.S.); 202114121@mail.sdu.edu.cn (Z.W.); 202120538@mail.sdu.edu.cn (Q.C.); 202034203@mail.sdu.edu.cn (Z.Q.)

² Department of Nanotechnology and Advanced Materials Engineering, Sejong University, Seoul 05006, Republic of Korea; kbkim@sejong.ac.kr

* Correspondence: weiminw@sdu.edu.cn

Abstract: The effect of the Cr element on the corrosion behavior of as-spun Fe_{72-x}Cr_xB_{19.2}Si_{4.8}Nb₄ ribbons with $x = 0, 7.2, 21.6,$ and 36 in 3.5% NaCl solution were investigated in this work. The results show that the glass formability of the alloys can be increased as Cr content (c_{Cr}) is added up to 21.6 at.%. When c_{Cr} reaches 36 at.%, some nanocrystals appear in the as-spun ribbon. With increasing c_{Cr} content, the corrosion resistances of as-spun Fe-based ribbons are continually improved as well as their hardness properties; during the polarization test, their passive film shows an increase first and then a decrease, with the highest pitting potential as $c_{Cr} = 7.2$ at.%, which is confirmed by an XPS test. The dense passivation film, composed of Cr₂O₃ and [CrO_x(OH)_{3-2x}, n H₂O], can reduce the number of corrosion pits on the sample surface due to chloride corrosion and possibly be deteriorated by the overdosed CrFeB phase. This work can help us to design and prepare the highly corrosion-resistant Fe-based alloys.

Keywords: Cr element; passivation; Fe based; amorphous alloys



Citation: Song, Z.; Wang, Z.; Chen, Q.; Qi, Z.; Kim, K.B.; Wang, W. Role of Cr Element in Highly Dense Passivation of Fe-Based Amorphous Alloy. *Materials* **2023**, *16*, 6630. <https://doi.org/10.3390/ma16206630>

Academic Editor: Tony Spassov

Received: 10 September 2023

Revised: 2 October 2023

Accepted: 4 October 2023

Published: 10 October 2023



Copyright: © 2023 by the authors. Licensee MDPI, Basel, Switzerland. This article is an open access article distributed under the terms and conditions of the Creative Commons Attribution (CC BY) license (<https://creativecommons.org/licenses/by/4.0/>).

1. Introduction

Since firstly fabricated in the last century, the amorphous alloys have a wide range of applications in many industrial fields, due to their special atomic structures, high strengths, and high hardness properties; Fe-based metallic amorphous alloys have especially excellent soft magnetic properties [1]. Meanwhile, Fe-based amorphous alloys are also used in various fields due to their excellent corrosion/wear resistances, such as drill bits [2] and artificial bone joints [3]. In addition, Fe-based metallic glasses contain major components with much lower costs than Co, Zr, Ni, Cu, and Ti [4]. Nowadays, in the rapid and high-level development of industry, it is necessary to solve the problems of corrosion and wear of metallic parts working in harsh environments to increase the corrosion resistances of Fe-based amorphous alloys is in line with the current industrial needs [5–7].

In the known stainless steels, Cr is one of the important and cheap elements to improve the corrosion resistance of the alloys [8]. Adding Cr can improve the corrosion/wear resistance of Fe-based amorphous alloys drastically [9–12]. At high temperatures, a high Cr content can ensure the mechanical strength and corrosion resistance of the alloys simultaneously, so a high-Cr alloy with high temperature corrosion resistance is widely used in the manufacturing of turbochargers, furnace fixtures, etc. [13,14]. The corrosion resistance performance of Fe-based amorphous alloys is attributed to three main factors: (1) amorphous alloys have a uniform passivation film [15]; (2) they have a high reactivity to diffuse the passive components to the surface [16]; and (3) they have no crystal defects. In biomedicine, the Cr-contained Fe-based amorphous alloys have excellent corrosion resistance and a superior biocompatibility, suitable for preparing surgical scissors. The (Fe,

Cr)-based glass exhibits better corrosion resistance than 316L steel and Ti-based commercial alloys in the human body-like environment [17,18]. The Fe-based amorphous alloys with Cr show high corrosion resistance in Cl^- environments, giving new ideas for the design of marine anti-corrosion alloys [2,19,20].

Mo is another important element to be often added to steel and cast iron to improve their corrosion resistance. According to the argument on the pitting resistance equivalent number (also denoted as PREM), the element Mo can increase the resistance to local pit corrosion of the alloy [21,22]. In the real preparation and machining process, some Mo is added to most stainless steels to improve their resistances to pitting corrosion. Generally, Mo has a high cost; other low cost elements are substituted and then reduce the cost of the alloys, keeping enough corrosion resistance [23]. In the alloys containing both Cr and Mo, Mo has a strong interaction with Cr to increase corrosion resistance, forming a Cr-rich passive oxide film, rather than forming a Mo-oxide film [24]. Thus, increasing the c_{Cr} , replacing Mo with other low-cost corrosion resistance elements in the alloy, is a practical idea [25]. It is necessary to be pointed out that Fe-based amorphous alloys can have a stable passivation rather than the active dissoluble film only when the Cr content is beyond a certain critical value [26]. Therefore, it is valuable to explore the role of the composition in the mechanism of formation and destruction of passivation films of Fe-based amorphous alloys in this work.

The marine environment contains lot of Cl^- and serious natural corrosion conditions. In a series of industrial circumstances, such as off-shore oil/gas exploitation and underwater operations, the selection of alloy types with high corrosion resistances is an important approach to solve the Cl^- -induced degradation of parts [27]. Recently, the effect of Cr mainly involves low Cr steel in case of CO_2 corrosion [28]; however, its anti-corrosion mechanism in different solutions is different. In this paper, we mainly studied the corrosion behavior of Fe-based amorphous alloys with Cr in a simulated marine environment, i.e., Cl^- -contained solution. At the same time, Mo in traditional Fe-based amorphous alloys containing Cr is replaced by Nb, Si, and other elements to improve the corrosion resistance and GFA of amorphous alloys. We discuss the effect of Cr on the corrosion behaviors of Fe-based amorphous alloys in neutral solutions. Meanwhile, the composition and destruction process of amorphous passivated films during electrochemical tests have been analyzed. The results of this work not only provide a new way to understand the effect of Cr on the corrosion resistance of Fe-based metallic glasses but also provide a new method for supplying the needed passivation film of Fe-based amorphous alloys.

2. Experimental

2.1. Sample Preparation

The alloy ingots with nominal compositions of $\text{Fe}_{72-x}\text{Cr}_x\text{B}_{19.2}\text{Si}_{4.8}\text{Nb}_4$ ($x = 0, 7.2, 21.6,$ and 36) were smelted with pure Fe (99.99 wt.%), pure Si (99.999 wt.%), pure Nb (99.99 wt.%), pure Cr (99.99 wt.%), and Fe-B ingots in an arc melting furnace (MAM-1 Edmund Buhler, Berlin, Germany) protected by high purity argon (99.999%). Each prepared ingot was 5 g and remelted at least four times during the smelting process to ensure the uniformity of the composition. The obtained ingots were made into amorphous ribbons at a roller speed of $41.8 \text{ m}\cdot\text{s}^{-1}$ under the protection of purified argon (99.999%) by a single roll melt spinning system (SD500 SKY, Shenyang, China).

2.2. Structural Analysis

The microstructures of the ingots and the as-spun ribbons as well as the ground ribbon powders were characterized by X-ray diffraction (XRD, Bruker D8 Discover, Beijing Technology Co., Ltd., Beijing, China). The thermodynamic behaviors of the ribbons were measured by differential scanning calorimetry (DSC, NETZSCH-404, Netzsch-404, Netzsch, Bavaria, Germany) under the protection of high purity argon at a heating rate of 20 K/min. The ribbon microstructures were observed by transmission electron microscopy (TEM, JEM-2100F, Japan Electronics Co., Ltd., Beijing, China), and the surface morphologies and

passivation film compositions were analyzed by a scanning electron microscope (SEM, JSM-7800 F Japan Electronics Co., Ltd., Beijing, China) and X-ray photoelectron spectroscopy (XPS, AXIS Supra, Manchester, UK).

2.3. Electrochemical Tests

An electrochemical workstation (CHI660E, Shanghai Chenhua Instrument Co., Ltd., Shanghai, China) was used to test and characterize the corrosion behavior of the ribbons at room temperature (300 K). The polarization curve and electrochemical impedance spectroscopy (EIS) of the ribbons were tested in 0.6 M NaCl neutral solution with a three-electrode system. One side of the ribbons was covered with silicone rubber 12 h in advance before the test to ensure the accuracy of the experiment. In addition, the ribbons were immersed in hydrochloric acid solution at pH = 3 for 215 h to calculate the weight loss rate, which was calculated by the following formula:

$$v_{\text{weight}} = \frac{m_0 - m_1}{S \times t} \quad (1)$$

m_0 (g) is the weight of the ribbon before immersion, m_1 (g) is the weight of the ribbon after immersion, S (cm²) is the immersion area of the ribbon, and t (h) is the immersion time.

3. Results and Discussion

Microstructure

Figure 1a–d shows the SEM images of the Fe_{72-x}Cr_xB_{19.2}Si_{4.8}Nb₄ ingots with $x = 0, 7.2, 21.6,$ and 36 , denoted by Cr0, Cr7, Cr21, and Cr36, respectively. The corresponding XRD patterns are shown in Figure 1e–h. Based on the XRD patterns, the four ingots had a certain similarity; there were α -Fe phases. With the addition of Cr, three strong peaks of α -Fe gradually shifted to the left, indicating that the average atomic distance increased, probably because Cr atoms with larger atomic radii replaced some of the Fe atoms. In addition, with the addition of the Cr element, CrFeB phases appeared in the ingots. Interestingly, from the ingots, the tendency of CrFeB phase dendritic growth was more and more evident. It was related to the migration and diffusion of solute during solidification, which was in line with the classical theory of “constitutional supercooling” proposed by Thiller [29]. In Cr0 ingot, the FeB phase presented in large plate-like shape (Figure 1a). With the addition of the Cr element, an elongated CrFeB phase began to appear in the ingot, indicating a strong binding force between Cr and Fe (Figure 1b,d). Some elliptical protrusions of Nb-Si intermetallic compounds in the ingots were formed, indicating that the strengths of Nb-Si bonds were stronger than those of Nb-Nb bonds (Figure 1c,d).

The microstructures of the Cr0, Cr7, Cr21, and Cr36 as-spun ribbons and the as-crushed Cr36 ribbon were investigated by XRD. The diffraction patterns of the as-spun Cr0, Cr7, and Cr21 ribbons exhibited a typical diffuse peak within the range of 44.2 ± 0.4 , without evident sharp crystallization peaks, indicating the amorphous properties of these samples (Figure 2a–c). This indicated that the FeSiBNb alloy with a small amount of Cr could form amorphous ribbons. As the Cr content increased, the position of the diffuse emission peak decreased from 44.6° to 43.2° , indicating an increase in the average atomic spacing, and the free volume within the ribbons also increased [30]. At the same time, the ribbons became increasingly brittle, and the XRD of the Cr36 ribbon showed evident crystal peaks. Cr36 ribbons became shorter and more brittle, which may have been related to the existence of internal stress during the ribbons production process. As shown in Figure 2d,e, there is a set of crystal peaks on the XRD curve of Cr36 ribbon; the α -Fe phase is not evident in the as-spun Cr36 ribbon, but the α -Fe peak becomes very evident after the sample has been crushed into pieces, similar to Ref. [31], indicating that the orientation of CrFeB and α -Fe are developed in the as-spun ribbon and that the α -Fe phase in the ingot also obtained a certain inheritance in the ribbons. These results suggested the structural heredity between the melts/glasses and ingots of present alloys.

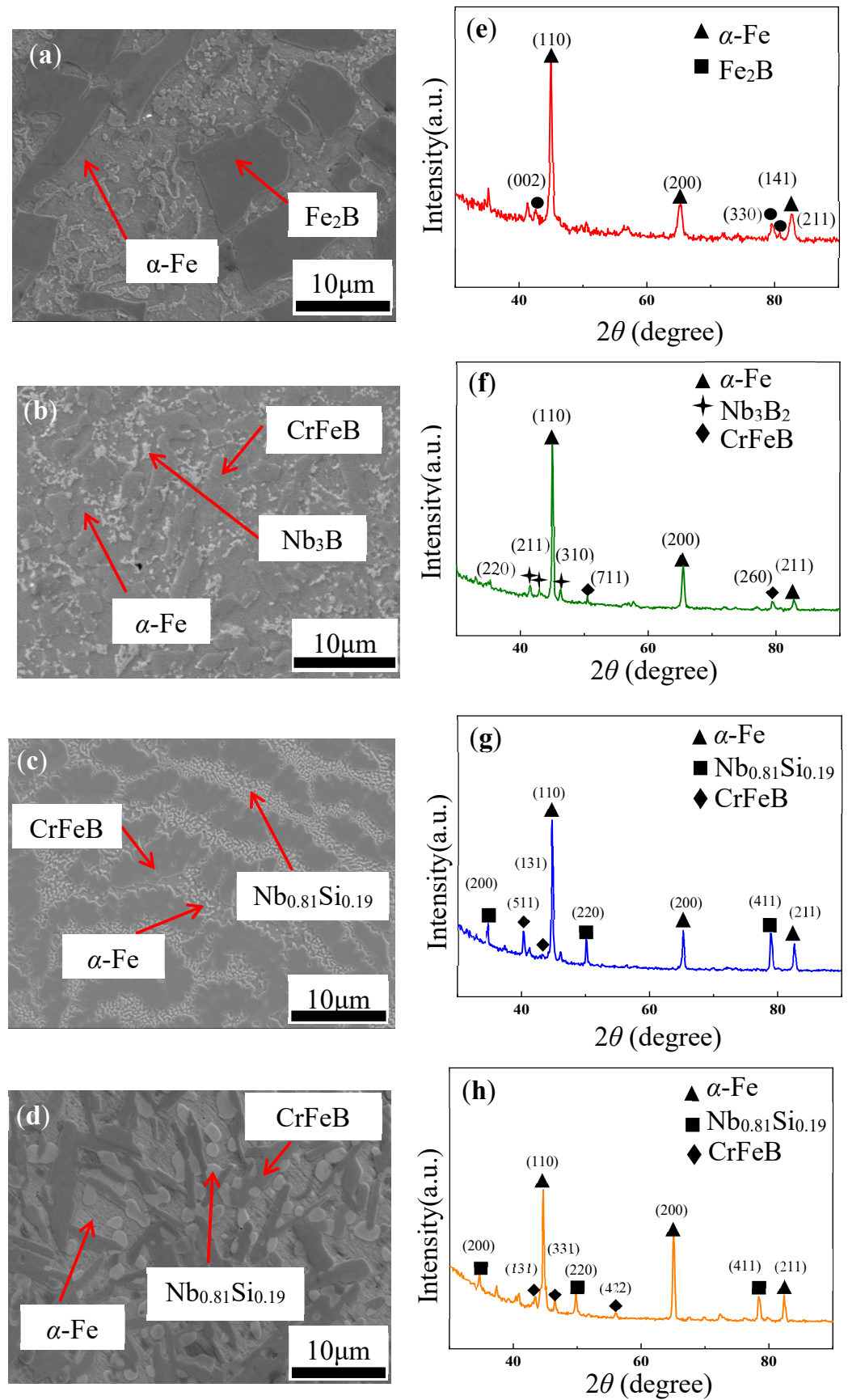


Figure 1. SEM micrographs of the $\text{Fe}_{72-x}\text{Cr}_x\text{B}_{19.2}\text{Si}_{4.8}\text{Nb}_4$. (a) $x = 0$ (Cr0), (b) $x = 7.2$ (Cr7), (c) $x = 21.6$ (Cr21), and (d) $x = 36$ (Cr36) ingots and XRD patterns of (e) Cr0, (f) Cr7, (g) Cr21, and (h) Cr36.

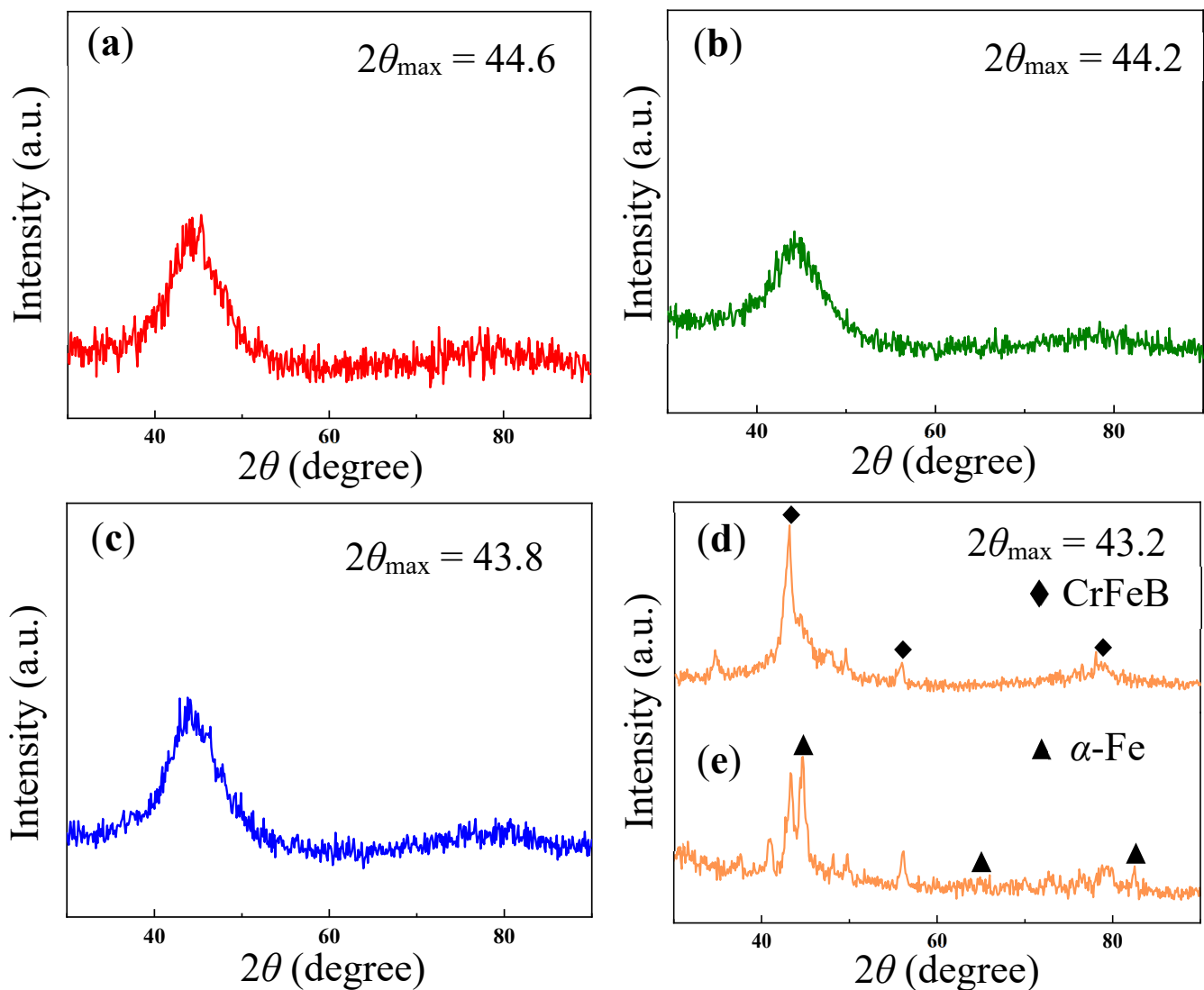


Figure 2. XRD curves of as-spun $\text{Fe}_{72-x}\text{Cr}_x\text{B}_{19.2}\text{Si}_{4.8}\text{Nb}_4$ ribbons together with a crushed sample. (a) $x = 0$ (Cr0) ribbon, (b) $x = 7.2$ (Cr7) ribbon, (c) $x = 21.6$ (Cr21) ribbon, (d) $x = 36$ (Cr36) ribbon, and (e) crushed Cr36 sample.

In order to further characterize the microstructure of the as-spun Cr36 ribbon, TEM tests were performed. The TEM images and selected area electron diffraction (SAED) patterns of Cr36 ribbon are shown in Figure 3. They present many nanocrystals in the Cr36 ribbon. As shown in Figure 3b,c, the grain diameter is about 100 nm, and there are some dislocation structures in the rod-shaped grains, which are distributed vertically along the head and tail of the rod-shaped grains. At the same time, EDS shows that the rod-shaped grains have oxygen enrichment, indicating that higher activation energy is displayed at the dislocations, and the metal oxide reaction preferentially occurs in the regions with high dislocation density [32]. Figure 3(d₁,d₂) are SAED corresponding to HRTEM (d) (High Resolution Transmission Electron Microscope), corresponding to the CrFeB and α -Fe phases, respectively.

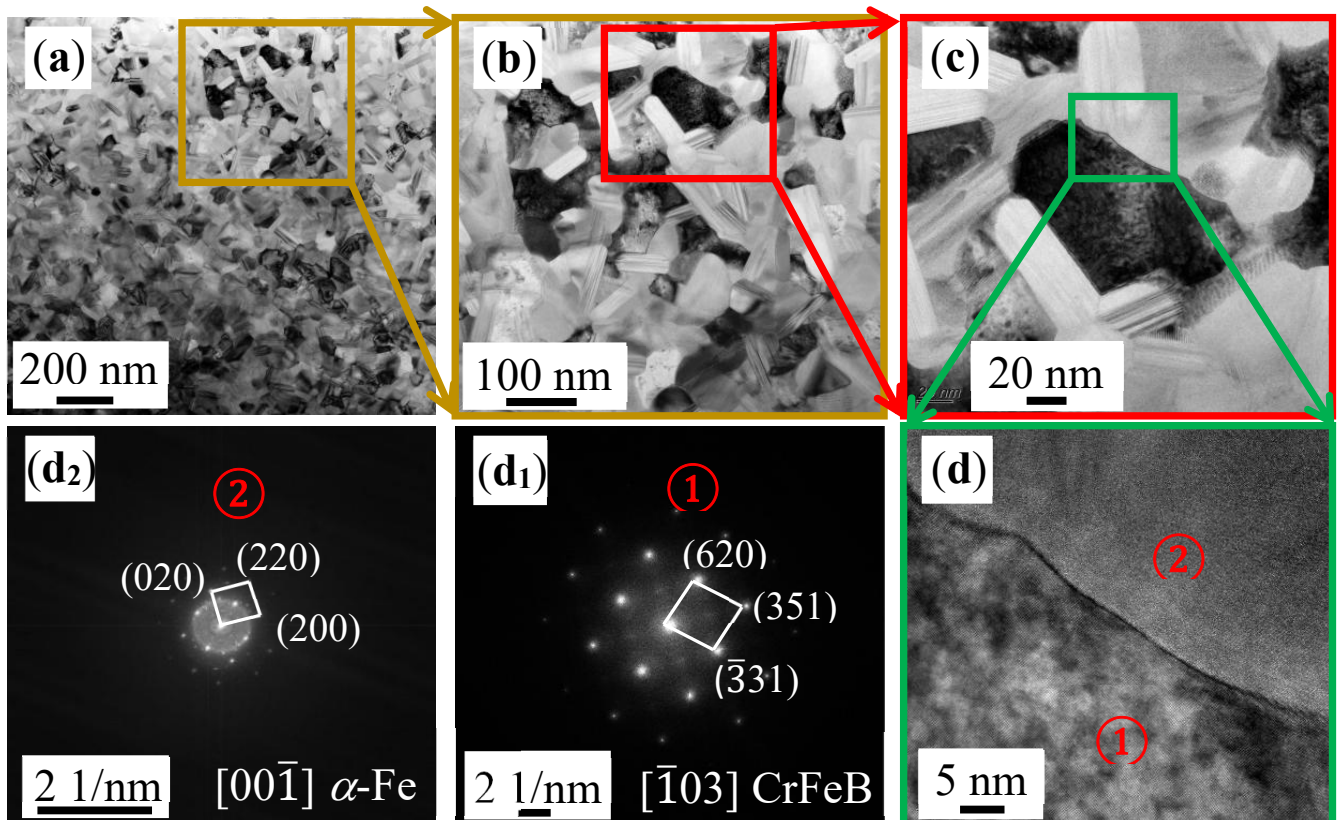


Figure 3. (a) LRTEM (Low Resolution Transmission Electron Microscope) image of $\text{Fe}_{36}\text{Cr}_{36}\text{B}_{19.2}\text{Si}_{4.8}\text{Nb}_4$ (Cr36). (b,c) are the enlarged part of (a); (d) is the HRTEM (High Resolution Transmission Electron Microscope) image of Cr36 (① and ② represent different phases); and (d₁) and (d₂) are the corresponding FFT (Fast Fourier Transform) patterns.

The DSC curves of the Cr0, Cr7, Cr21, and Cr36 ribbons with heating/cooling rates of 20 K/min are shown in Figure 4. The characteristic thermodynamic temperatures are listed in Table 1. The amorphous Cr0, Cr7, and Cr21 ribbons exhibit similar exothermic behaviors, and all the amorphous samples have only one exothermic crystallization peak, usually corresponding to eutectic crystallization [33]. The height of the crystallization peak increases with the increase in Cr content. As the Cr content increases up to 21.6 at.%, the reduced crystallization temperature T_{rx} ($=T_x/T_1$) and ΔH_{rc} of amorphous ribbons also gradually increases, indicating that the addition of 21.6 at.% Cr element can still improve the amorphous stability and amorphous formation ability of Fe-based ribbons [34]. When the addition of the Cr element reaches 36 at.%, there is no exothermic peak in the sample in Figure 4a, indicating that the ribbons has crystallized. In addition, the onset temperature of melting (T_m) of the amorphous ribbons shows an increasing trend, and the end temperature of melting (T_1) does not tends to decrease with increasing x (Figure 4b). In other words, the solidification temperature range ΔT_1 ($T_1 - T_m$) of ribbons does not change monotonically. The results show that Cr21 ribbon is the closest component to the eutectic point [30].

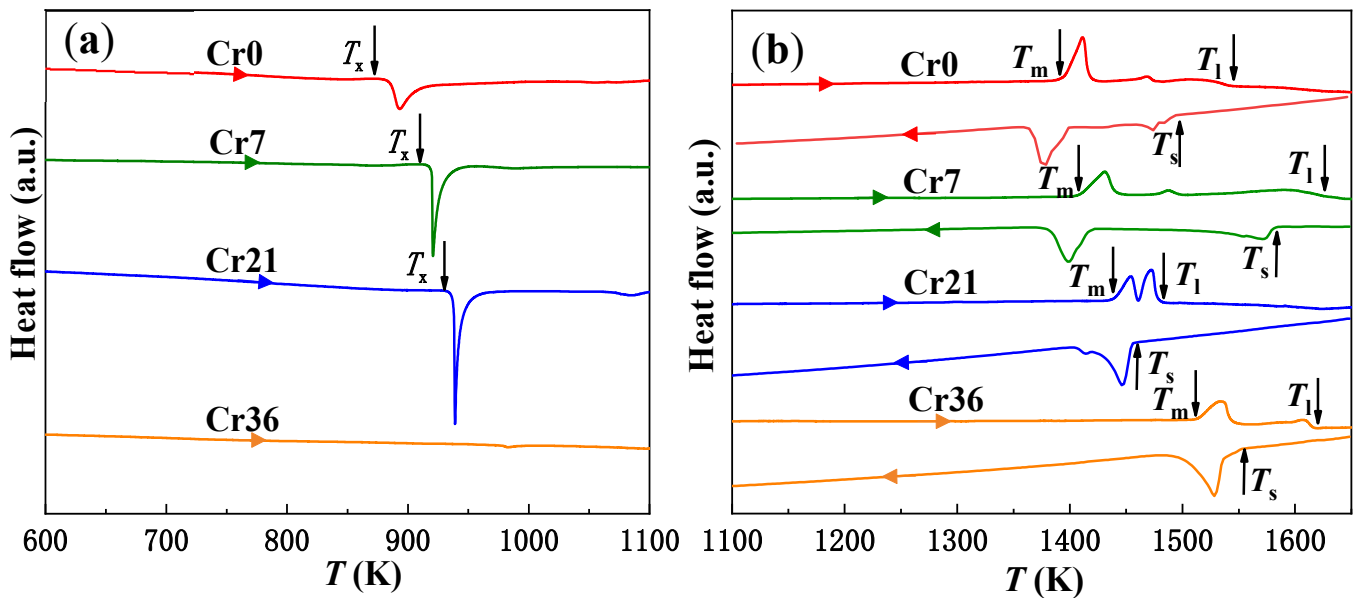


Figure 4. DSC curves of $\text{Fe}_{72-x}\text{Cr}_x\text{B}_{19.2}\text{Si}_{4.8}\text{Nb}_4$ with $x = 0$ (Cr0), $x = 7.2$ (Cr7), $x = 21.6$ (Cr21), and $x = 36$ (Cr36) ribbons at different temperature intervals. (a) Heating curves in 600–1100 K with 20 K/min, and (b) heating and cooling curves in 1100–1650 K.

Table 1. Thermal parameters deduced from the DSC curves, including the onset crystallization temperature T_x , the solidification temperature T_s , the onset melting temperature T_m , the liquidus temperature T_l , the solidification temperature range $\Delta T_1 (=T_l - T_m)$, the reduced crystallization $T_{rx} (=T_x/T_l)$, the degree of supercooling $\Delta T (=T_l - T_s)$, and the reduced crystallization heat $\Delta H_{rc} (= \Delta H_c / \Delta H_m)$. Here, ΔH_c and ΔH_m are heats of crystallization and melting, respectively.

Ribbon	T_x (K)	T_s (K)	T_m (K)	T_l (K)	ΔT_1 (K)	ΔT (K)	T_{rx}	$\Delta H_{rc} (\Delta H_c / \Delta H_m)$
$x = 0$	882	1492	1394	1541	147	49	0.57	0.18
$x = 7.2$	916	1580	1406	1619	213	39	0.57	0.23
$x = 21.6$	933	1459	1438	1482	44	23	0.63	0.52
$x = 36$	-	1554	1512	1615	103	61	-	-

In general, the smaller the residual penetration depth, the higher the nanohardness. The steeper the unloading curve, the larger the Young's modulus [35–37]. The nanoindentation images of Cr0, Cr7, Cr21, and Cr36 ribbons are shown in Figure 5, with the increase in Cr content, the hardness and Young's modulus of the ribbons both increased. The hardness and Young's modulus of the Cr36 ribbon as a crystal increase significantly, indicating that Cr-rich ordered clusters in the ribbon can improve the hardness of the ribbon.

Figure 6 shows the potentiodynamic polarization plots of the Cr0, Cr7, Cr21, and Cr36 as-spun ribbons and the corrosion rate R_{im} deduced from the weight loss in the HCl solution with a pH = 3. The corrosion potential E_{corr} (vs. SCE (saturated calomel (reference) electrode)), corrosion current density i_{corr} ($\mu\text{A}\cdot\text{cm}^{-2}$), pitting potential E_{pit} (V vs. SCE), and deduced corrosion rate CR ($\mu\text{m}\cdot\text{y}^{-1}$) with Equation (2) are summarized in Table 2 [38,39].

$$\text{CR} = 3.28 i_{\text{corr}} \times M/nd \text{ (}\mu\text{m} \times \text{y}^{-1}\text{)} \quad (2)$$

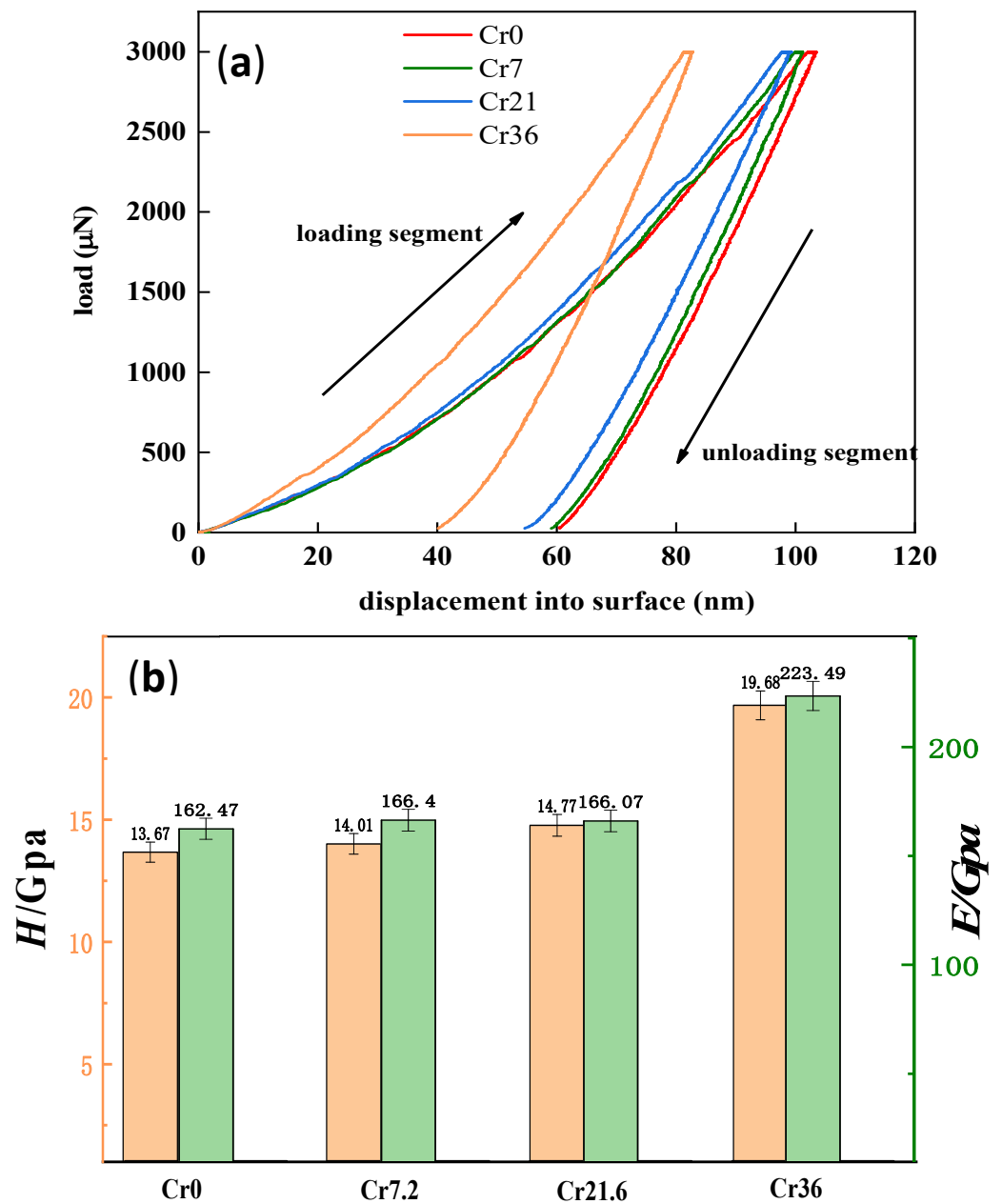


Figure 5. Nanoindentation of $\text{Fe}_{72-x}\text{Cr}_x\text{B}_{19.2}\text{Si}_{4.8}\text{Nb}_4$ with $x = 0$ (Cr0), $x = 7.2$ (Cr7), $x = 21.6$ (Cr21), and $x = 36$ (Cr36) ribbons: (a) Curve of the load and indentation depth; (b) calculated results of the nanoindentation, including hardness and modulus.

Table 2. Parameters deduced from potentiodynamic polarization plots in Figure 6, such as corrosion potential E_{corr} (V vs. SCE), corrosion current density i_{corr} ($\mu\text{A}\cdot\text{cm}^{-2}$), pitting potential E_{pit} (V vs. SCE), and deduced corrosion rate CR ($\mu\text{m}\cdot\text{y}^{-1}$).

Ribbon	E_{corr} (V)	i_{corr} ($\mu\text{A}\cdot\text{cm}^{-2}$)	E_{pit} (V)	CR ($\mu\text{m}\cdot\text{y}^{-1}$)
$x = 0$	−0.69	40.72	−0.60	473
$x = 7.2$	−0.56	14.83	1.21	172
$x = 21.6$	−0.55	8.43	1.04	98
$x = 36$	−0.50	5.28	0.68	61

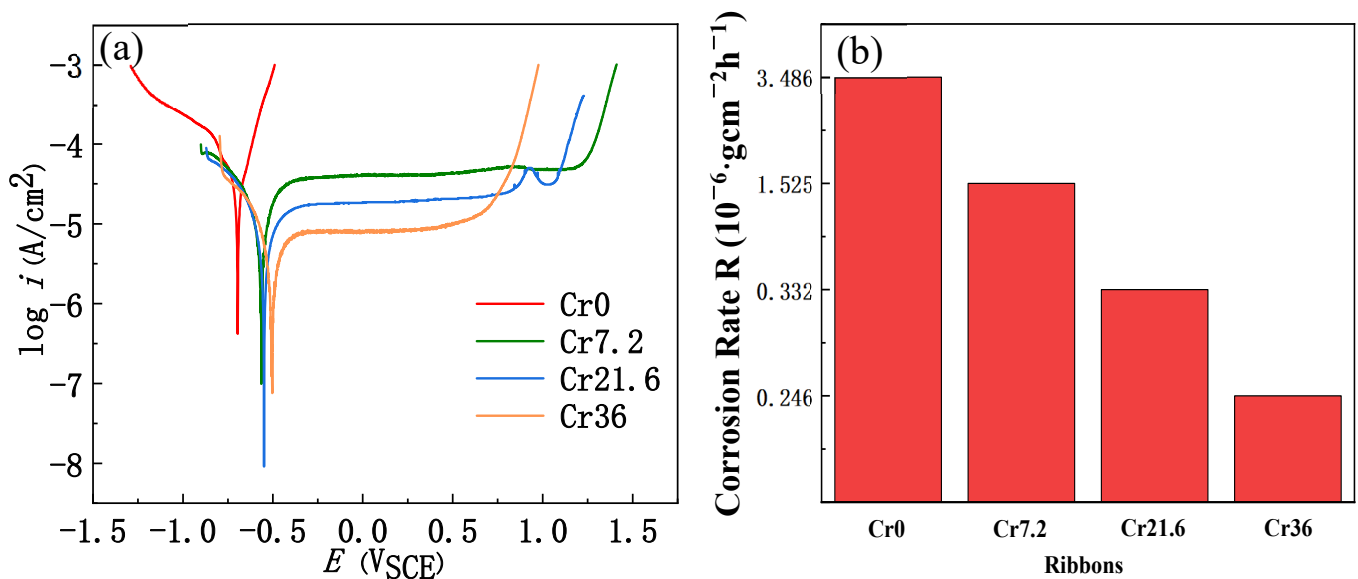


Figure 6. (a) Potentiodynamic polarization plots of as-spun ribbons $\text{Fe}_{72-x}\text{Cr}_x\text{B}_{19.2}\text{Si}_{4.8}\text{Nb}_4$ with $x = 0$ (Cr0), $x = 7.2$ (Cr7), $x = 21.6$ (Cr21), and $x = 36$ (Cr36) in neutral solutions. (b) Corrosion rate R_{im} derived from weight loss obtained by immersing in acid solution.

Here, M is the atomic weight of Fe (55.85 g), n is the number of electrons transferred in the corrosion reaction ($n = 2$), and d is the density of Fe (7.88 g cm^{-3}). For the sake of similarity, the corrosion rate is mainly ascribed to the dissolution of Fe atoms.

From the potentiodynamic polarization curves (Figure 6a), the amorphous ribbon Cr0 has no evident passivation platform, the anode polarization curves of Cr7, Cr21, and Cr36 have significantly wide passivation platforms, and there is no evident anodic Tafel region. The corrosion current density was determined by cathodic polarization curves and corrosion potential. In addition, the addition of Cr increased the corrosion potential of the ribbons and decreased the corrosion current density of the ribbons (Table 2). As can be seen from Figure 6b, with the increase in Cr content, the corrosion rate of the ribbons after immersing in HCl solution with pH = 3 for 215 h decreased, which was consistent with the Tafel curves. At a high potential of about 0.7 V, Cr transpassive dissolution occurred in Cr36 ribbon, according to Ref. [40], resulting in a gradual increase in current. When the potential was less than 0, with the increase in c_{Cr} (Table 2), the value of i_{corr} and E_{corr} of the ribbons decreased, which was consistent with Figure 6b, indicating that the corrosion resistance of the ribbons was getting better. When the potential was increased until the ribbons were pitted, it can be seen that the E_{pit} of the ribbons reached the maximum value in Cr7, indicating that Cr7 had the best pitting corrosion resistance. On the one hand, the disorder of amorphous ribbons reduced the existence of crystal defects and prevented the formation of galvanic corrosion. On the other hand, the composition contained more easily passivated elements (such as Cr), which was conducive to improving corrosion resistance [41].

In comparison, we collect the data of 51 Fe-based glassy alloys, as shown in Figure 7. The i_{corr} and E_{corr} of Fe-based glassy alloys are listed in Table S1. Apparently, Cr36 has a very low i_{corr} and a certain positive E_{corr} , showing a super corrosion resistance.

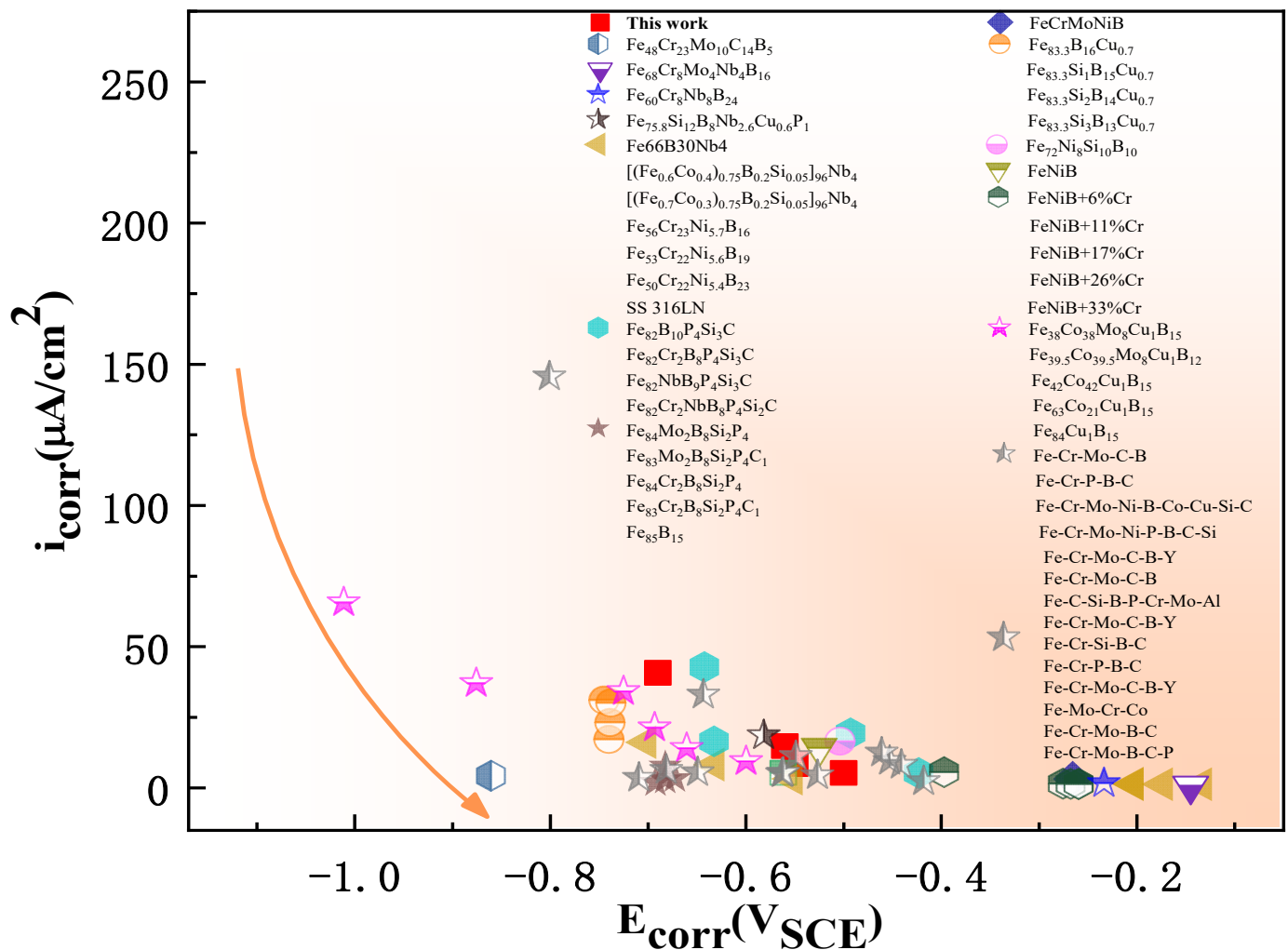


Figure 7. The comparison diagram of corrosion potential (E_{corr}) and corrosion current density (i_{corr}) of various Fe-based alloys in 3.5 wt.% NaCl solution; details are listed in Table S1 [42–53].

Figure 8 shows the surface schematic graph morphologies and cross-sections of the tested samples after the polarization corrosion experiment in the neutral solution. In the case of Cr0, a corrosion scale in the thickness of 1–2 μm (Fe_2O_3 and SiO_2) was mostly detached, with only small amounts remaining, and evident stress cracking was observed on the surface, exposing the matrix under the scale. In contrast, very little corrosion product was observed over the smooth surface of Cr7 (Figure 8b). It is thought that a relatively Cr-rich passive oxide may be produced on the surface, indicating that adding a small amount of Cr element can reduce the occurrence of local corrosion pits [54]. However, corrosion pits on the Cr21 ribbon's surface are more evident than Cr7. At this time, small pits are easily formed on the bottom of the early formed large pit. On the surface of the Cr36 ribbon, it can be observed that the ribbon surface is rougher than Cr21 (Figure 8d), and the surface passivation film caused by pitting corrosion is in a chain-like shape. These results show that the addition of Cr element can firstly reduce stress cracking and pitting by corrosion and then increase them, show a maximal pitting resistance at $c_{\text{Cr}} = 7$ at.%.

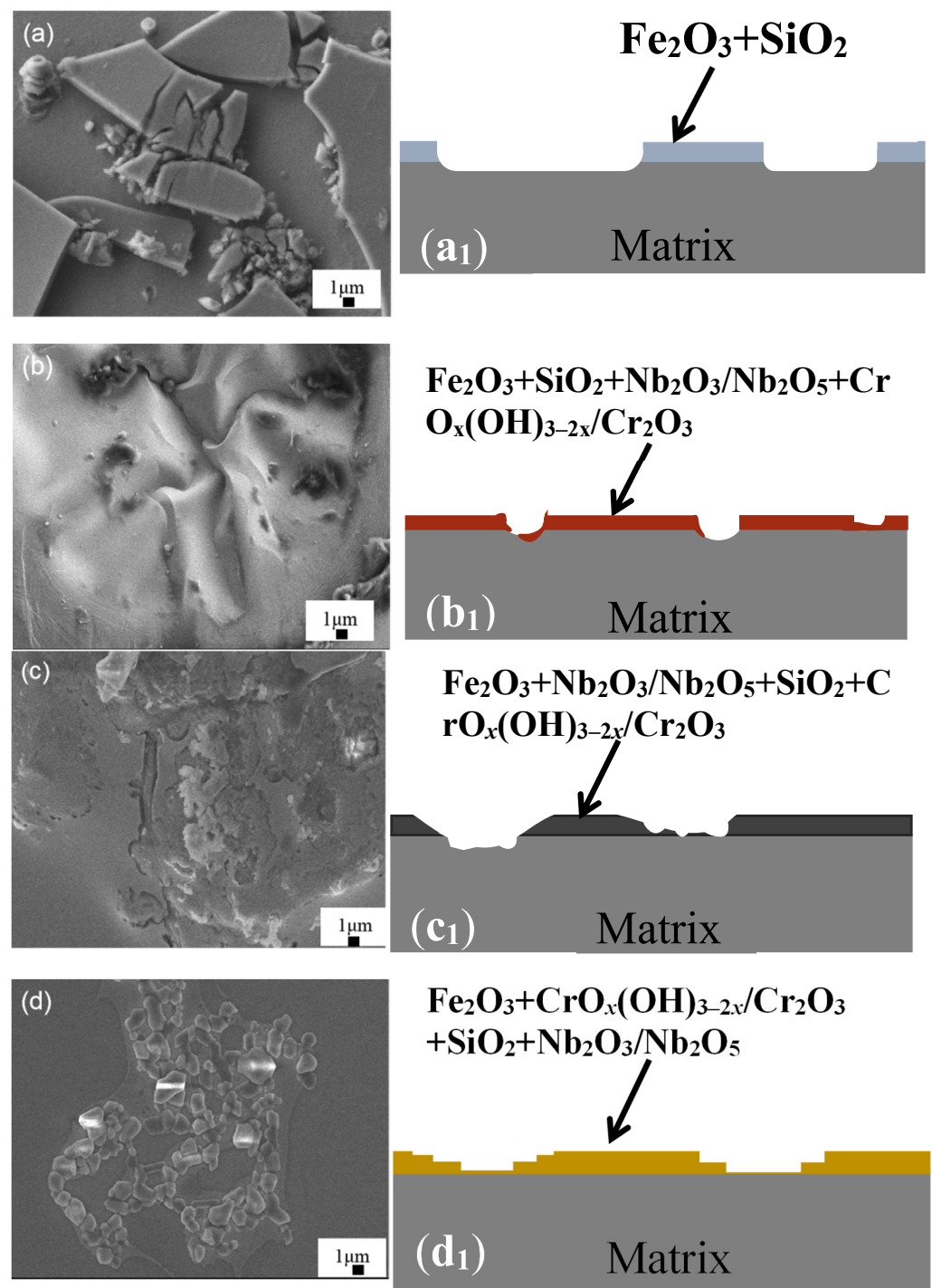


Figure 8. SEM images and simplified cross-sectional schematics of corroded $\text{Fe}_{72-x}\text{Cr}_x\text{B}_{19.2}\text{Si}_{4.8}\text{Nb}_4$ samples. (a) $x = 0$ (Cr0). (b) $x = 7.2$ (Cr7). (c) $x = 21.6$ (Cr21). (d) $x = 36$ (Cr36). (a₁–d₁) Simplified cross-section schematics showing their damaged characteristics.

To further understand the surface property changes, Figure 9 displays the XPS etching analysis on the surfaces of the $\text{Fe}_{72-x}\text{Cr}_x\text{B}_{19.2}\text{Si}_{4.8}\text{Nb}_4$ ribbons with $x = 0, 7.2, 21.6,$ and 36 after the potentiodynamic polarization in neutral solution. On the Fe 2p spectra (Figure 9(a₀–a₃)), the XPS curves of four ribbons can be decomposed into two peaks at about 707 and 709/710 eV, being identified as Fe^0 and $\text{Fe}^{2+}/\text{Fe}^{3+}$, respectively [55]. As can be seen from Figure 8(a₀,a₁), the Fe^{3+} peak at 709.9 eV in Cr0 and Cr7 tend to decrease with the increase in etching time, whereas the $\text{Fe}^{3+}/\text{Fe}^{2+}$ peak at 709.3/710 eV in Cr21 and Cr36

gradually increases, which is because the passivation films of the Cr21 and Cr36 are thicker and denser. Under the same etching time, the passivation films of Cr36 are still Fe^{2+} ; there is no conversion of Fe^{2+} to Fe^{3+} , which is consistent with the low corrosion current density and high corrosion potential shown in the Tafel curve (Figure 6a), indicating that a dense passivated film containing Fe is formed on its surface and that the Fe element finally has experienced interactive oxidation in the passivation film.

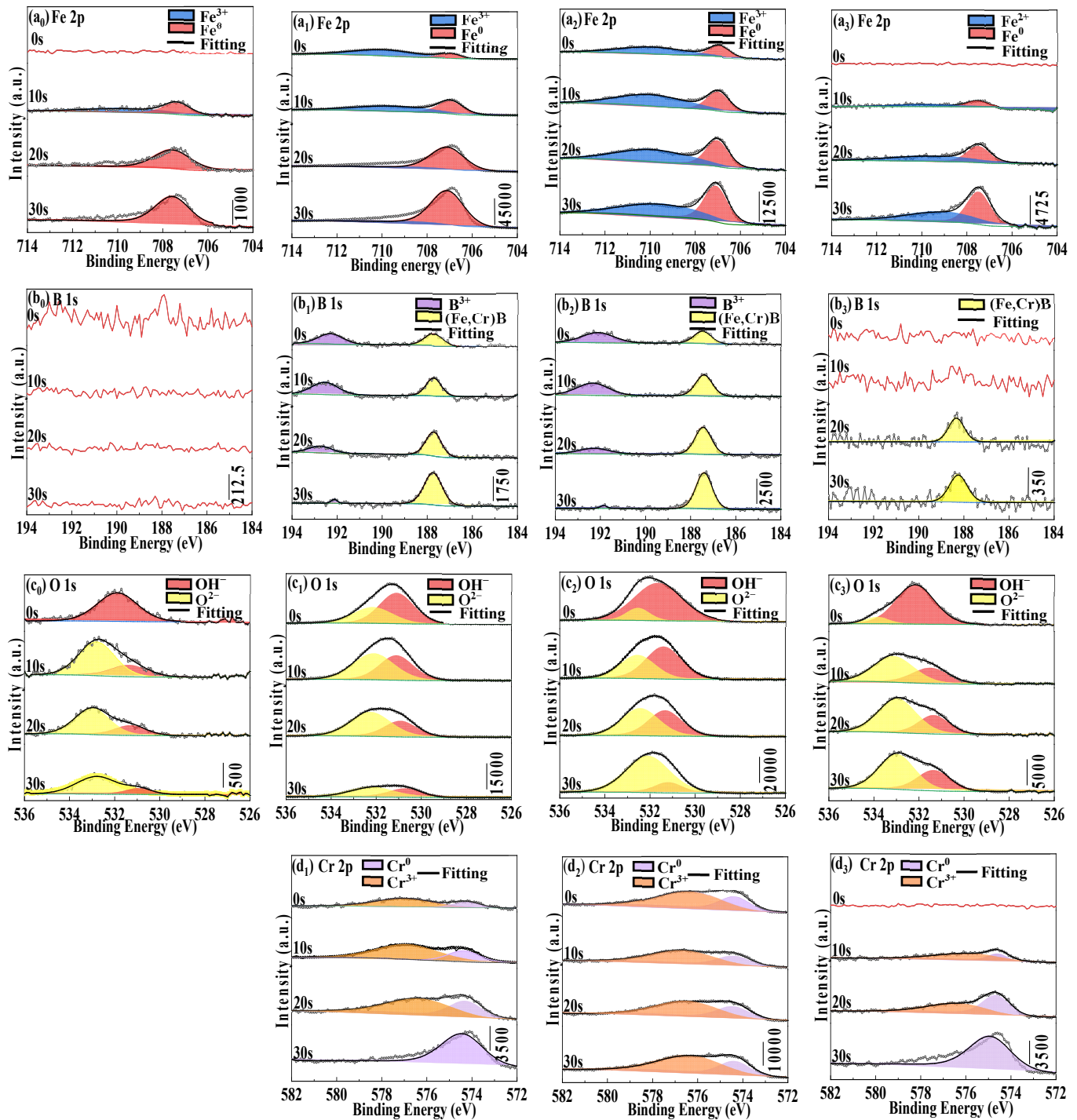
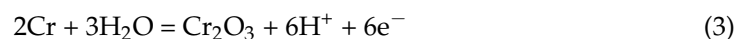


Figure 9. XPS spectra of Fe 2p (a₀–a₃), B 1s (b₀–b₃), O 1s (c₀–c₃) and Cr 2p (d₁–d₃) in binding energy regions for the as-spun $\text{Fe}_{72-x}\text{Cr}_x\text{B}_{19.2}\text{Si}_{4.8}\text{Nb}_4$ ribbons with $x = 0$ (Cr0), $x = 7.2$ (Cr7), $x = 21.6$ (Cr21), and $x = 36$ (Cr36) after corrosion in neutral solutions.

On most B 1s spectra (Figure 9(b₀–b₃)), we can decompose the XPS curves into two peaks at 192 and 188 eV, being indexed as B³⁺ and (Fe, Cr)B, respectively. It can be seen from Figure 9(b₀–b₃) that the oxides of the B element only exist on the surfaces of Cr7 and Cr21, and the contents of oxides are small; the (Fe, Cr)B compounds peak are stronger, and exist in Cr7, Cr21 and Cr36. Figure 9(b₀–b₃) shows that most of the element B oxides are corroded away during the corrosion process, indicating that element B is not the main factor in improving the corrosion resistance of the ribbons.

On the O 1s spectra, the XPS curves can be decomposed two peaks at about 531 and 532 eV, identified as OH[−] (531.3 eV) and O^{2−} (532.9 eV), respectively [56]. With the increase in etching time, the reduction rate of OH[−] of the four ribbons is greater than the reduction rate of O^{2−}, indicating that some O^{2−} still exists at a certain depth of etching and passivation film composed of Fe₂O₃ and Cr₂O₃, and a certain amount of Si, Nb, and B element oxides is formed on the surface of the sample. Meanwhile, the oxide thickness of Cr7 and Cr21 is much higher than Cr0 and Cr36, due to their higher amorphous fraction *f_a* (Figure 4a).

On the Cr 2p spectra, we can divide the XPS curve into two peaks, identified as Cr⁰ (574.1 and 583.5 eV) and Cr³⁺ (577 and 586.4 eV), respectively, according to Refs. [57,58]. For Fe-based amorphous ribbons containing corrosion-resistant elements such as Cr, the surface of the amorphous ribbons will form a passivation film containing corrosion resistant elements, which will improve the corrosion resistance [59]. Cr is easy to form passivation films of chromium oxide and chromium hydroxide on the surfaces of amorphous ribbons, thus protecting the amorphous phase and inhibiting the active dissolution of the amorphous phase [60]. The formation mechanism can be explained by the following equation:



Then, part of the Cr oxide will further form H₂O and Cr hydroxide [CrO_{*x*}(OH)_{3−2*x*}, *n*H₂O]; both oxide films can improve the resistance of the ribbons to chloride ion corrosion [61].

As can be seen from Figure 9, Figure S1 and S2, the passivation film thicknesses of Cr7 and Cr21 ribbons are slightly larger than those of a Cr36 ribbon; among them, Cr21 has the best amorphous formation ability, so a thicker passive layer is formed on the surface. As can be seen from Figure 6a, Cr7 has a strong pitting corrosion resistance and is more stable, indicating that the oxide thickness is not the sole factor for its stability. However, it can be seen from the *i_{corr}* and *E_{corr}* of Cr36 in Table 2 that the corrosion resistance of Cr36 is still the best, indicating that a dense passivation film is formed on the surface of Cr36 when the potential is lower than 0 V.

Figure 10 shows the Nyquist and Bode plots with fitting results of Fe_{72−*x*}Cr_{*x*}B_{19.2}Si_{4.8}Nb₄ glassy ribbons with *x* = 0, 7.2, 21.6, and 36 in a neutral solution. Among several equivalent circuit candidates, the equivalent circuit R(Q(R(CR))) is suitable for fitting the EIS data. The non-ideal capacitive behavior due to local inhomogeneity is represented by the constant phase element CPE (*Q*). The impedance of a CPE is defined as [62–64]:

$$Q = (j\omega)^{-n} / Y_0 \quad (4)$$

Here, *Y*₀ is the frequency independent parameter (Ω^{−1}cm^{−2}s^{*n*}), *j* is the imaginary number, *ω* is the angular frequency (rad s^{−1}), and *n* indicates the CPE power, which is between 0.5 and 1. When *n* = 1, the *Q* describes a pure capacitor. For 0.5 < *n* < 1, the *Q* represents a distribution of dielectric relaxation times in the frequency domain, and *Q* represents a Warburg impedance with diffusion character (*n* = 0.5).

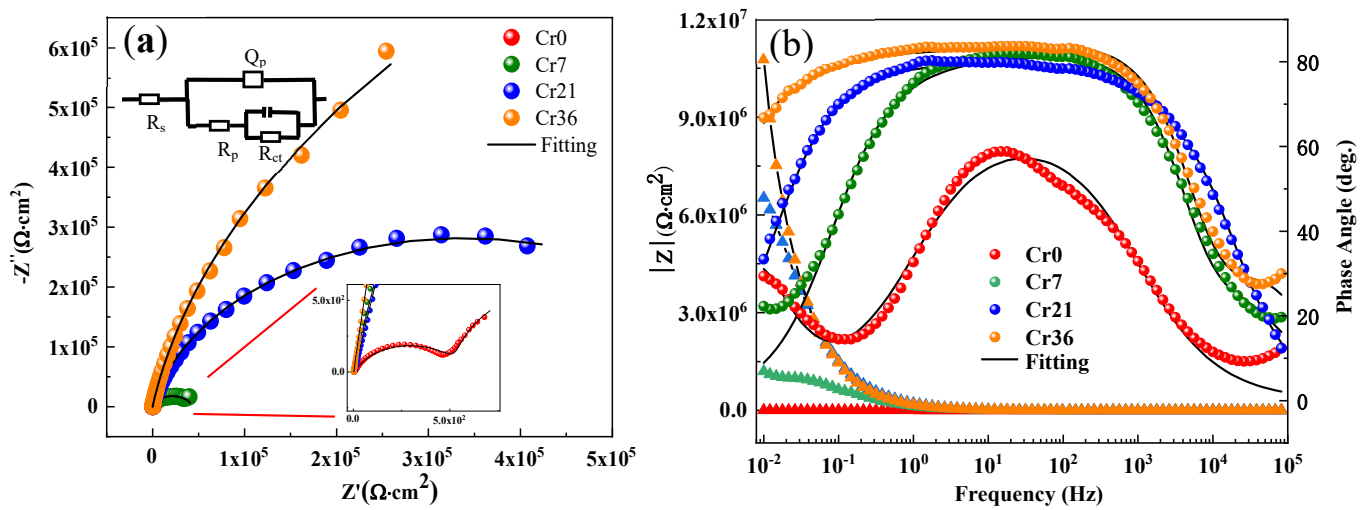


Figure 10. (a) Nyquist plots of as spun $\text{Fe}_{72-x}\text{Cr}_x\text{B}_{19.2}\text{Si}_{4.8}\text{Nb}_4$ ribbons with $x = 0$ (Cr0), 7.2 (Cr7), 21.6 (Cr21), and 36 (Cr36) in neutral solution with equivalent circuits $R(Q(R(CR)))$ and (b) the corresponding Bode plots. Symbols show the experimental data while solid lines are fitting results.

The fitting results are summarized in Table 3. Here, the change transfer resistances (R_{ct}) of the ribbons increase from 1.1 to 2410 $\text{k}\Omega\cdot\text{cm}^2$ with the increase in c_{Cr} , indicating that the passivation film becomes more stable and dense, which is consistent with Ref. [65]. Meanwhile, we can see that the value of n ranges from 0.83 to 0.88. The n value of the Cr0 ribbon is low, which indicates a higher dispersion at the alloy/electrolyte interface, probably due to the defects on the passive film formed in this hypersaline solution [66,67]. With increasing c_{Cr} , the diameter of the Nyquist semicircle of Fe-based glassy ribbons significantly expands to the larger size (Figure 10a). The Bode plots is mainly divided into three different regions: (i) the low frequency region (10^{-2} –1 Hz) mainly reflects the capacitance and resistance at the interface between the ribbons and the passivation film; (ii) the intermediate frequency region (1– 10^3 Hz) mainly reflects the resistance and capacitance of the passivation film; and (iii) the high frequency region (10^2 – 10^5 Hz) in this work mainly reflects the capacitances and resistances of the corrosion products [68–70]. In the bode plots, the closer the phase angle is to 90° , the more stable and compact the passivation film on the corrosion surface of the ribbons will be; it can be seen that the phase angle of the ribbons in the intermediate frequency region is closer to 90° when the element Cr is added [71]. Therefore, it can be seen that the increase in Cr content can make the passivation film more dense and thick, which is consistent with the passivation platform and the corrosion current density i_{CORR} on the dynamic potential polarization curve (Figure 6a). The total resistance after fitting increases with the increase in Cr content, which is consistent with the Tafel results (Figure 6a).

Table 3. Simulated parameters of the $\text{Fe}_{72-x}\text{Cr}_x\text{B}_{19.2}\text{Si}_{4.8}\text{Nb}_4$ ribbons with $x = 0, 7.2, 21.6,$ and $36,$ derived from EIS curves. R_s : the solution resistance, Q_p : the passive film capacitance, R_p : the passive film resistance, and R_{ct} : the charge transfer resistance.

Ribbon	$R_s(\Omega\cdot\text{cm}^2)$	Q_p		R_p ($\text{k}\Omega\cdot\text{cm}^2$)	C ($\mu\text{F}\cdot\text{cm}^2$)	R_{ct} ($\text{k}\Omega\cdot\text{cm}^2$)	R_{total} ($\text{k}\Omega\cdot\text{cm}^2$)
		$\gamma(10^{-5} \Omega^{-1}\text{s}^n\text{cm}^{-2})$	n				
$x = 0$	3.5	50.6	0.72	0.5	31,790	1.1	1.7
$x = 7.2$	1.1	3.3	0.84	0.0	9.8	43.0	43.0
$x = 21.6$	3.0	1.2	0.88	0.1	0.4	678.6	678.7
$x = 36$	1.3	1.1	0.86	3.2×10^{-3}	6.0	2410	2410

4. Conclusions

In this work, we prepared $\text{Fe}_{72-x}\text{Cr}_x\text{B}_{19.2}\text{Si}_{4.8}\text{Nb}_4$ ingots with $x = 0, 7.2, 21.6$, and 36 by arc melting, and ribbons with melt spinning in a vacuum. The microstructures of the ingots were investigated; microstructure investigations, hardness tests, electrochemical experiments, and XPS analyses on ribbons were conducted; and the surface morphologies of the ribbons after testing were analyzed. Combining the heredity between the ingots and ribbons, the effect of the Cr element on the properties of the Fe-based amorphous alloys could be found, as follows:

- (1) With increasing Cr content $c_{\text{Cr}}(x)$, the stability and glass formability (GFA) of Fe-based alloys firstly increased until $x = 21$ and then decreased drastically as $x = 36$. Simultaneously, the CrFeB phase and clusters in the samples tended to form with strong orientations in the ingots and as-spun ribbons, which deteriorated the GFA of the alloy, as its abundance was high enough.
- (2) With increasing c_{Cr} , the corrosion rate R_{im} , corrosion current i_{corr} , and deduced corrosion rate CR of Fe-based ribbons increased monotonically, as well as their hardness, whereas their pitting resistance increased until $x = 7$ and decreased as $x = 21$, indicating that the most stable passive film formed at a proper c_{Cr} , which was confirmed by XPS data. This work can give a new clue to design and prepare highly corrosion-resistant Fe-based alloys.

Supplementary Materials: The following supporting information can be downloaded at: <https://www.mdpi.com/article/10.3390/ma16206630/s1>. Figure S1: XPS spectra of Si 2p and Nb 3d in binding energy regions for the as-spun $\text{Fe}_{72-x}\text{Cr}_x\text{B}_{19.2}\text{Si}_{4.8}\text{Nb}_4$ ribbons with $x = 0$ (Cr0), $x = 7.2$ (Cr7), $x = 21.6$ (Cr21), and $x = 36$ (Cr36) after corrosion in neutral solutions; Figure S2: XPS spectra of Fe 2p, Si 2p, B 1s, Nb 3d O 1s and Cr 2p in binding energy regions for the as-spun $\text{Fe}_{72-x}\text{Cr}_x\text{B}_{19.2}\text{Si}_{4.8}\text{Nb}_4$ ribbons with $x = 0$ (Cr0), $x = 7.2$ (Cr7), $x = 21.6$ (Cr21), and $x = 36$ (Cr36); Table S1: The comparison data of corrosion potential (E_{corr}) and corrosion current density (i_{corr}) of various Fe-based alloys in 3.5 wt.% NaCl solution.

Author Contributions: Z.S.: Conceptualization, Methodology, Validation, Data curation, Investigation, Formal analysis, Writing—original draft, Writing—review & editing. Z.W.: Methodology, Formal analysis. Q.C.: Methodology, Validation. Z.Q.: Methodology, Supervision. K.B.K.: Software, Formal analysis. W.W.: Conceptualization, Formal analysis, Writing—review & editing, Supervision, Funding acquisition. All authors have read and agreed to the published version of the manuscript.

Funding: This work was financially supported by the key research and development program of China (Grant No. 2022YFB2404102), the National Natural Science Foundation of China (51971093, 52171158, and 52101196), the Open Project Program of Shandong Marine Aerospace Equipment Technological Innovation Center (Ludong University) (Grant No. MAETIC2021-11), and the Key R&D Program of Shandong Province, China (Grant No. 2021ZLGX01 and 022CXGC020308).

Institutional Review Board Statement: Not applicable.

Informed Consent Statement: Not applicable.

Data Availability Statement: Data available on request due to restrictions eg privacy or ethical. The data presented in this study are available on request from the corresponding author. The data are not publicly available due to follow-up research on the work.

Conflicts of Interest: The authors declare no conflict of interest.

References

1. Lee, C.-Y.; Lin, T.-J.; Sheu, H.-H.; Lee, H.-B. A study on corrosion and corrosion-wear behavior of Fe-based amorphous alloy coating prepared by high velocity oxygen fuel method. *J. Mater. Res. Technol.* **2021**, *15*, 4880–4895. [[CrossRef](#)]
2. Farmer, J.; Choi, J.-S.; Saw, C.; Haslam, J.; Day, D.; Hailey, P.; Lian, T.; Rebak, R.; Perepezko, J.; Payer, J.; et al. Iron-Based Amorphous Metals: High-Performance Corrosion-Resistant Material Development. *Metall. Mater. Trans. A* **2009**, *40*, 1289–1305. [[CrossRef](#)]

3. Ibrahim, M.Z.; Sarhan, A.A.D.; Kuo, T.Y.; Yusof, F.; Hamdi, M.; Lee, T.M. Developing a new laser cladded FeCrMoCB metallic glass layer on nickel-free stainless-steel as a potential superior wear-resistant coating for joint replacement implants. *Surf. Coat. Technol.* **2020**, *392*, 125755. [[CrossRef](#)]
4. Souza, C.A.C.; Ribeiro, D.V.; Kiminami, C.S. Corrosion resistance of Fe-Cr-based amorphous alloys: An overview. *J. Non-Cryst. Solids* **2016**, *442*, 56–66. [[CrossRef](#)]
5. Montemor, M.F.; Simões, A.m.p.; Ferreira, M.G.S.; Belo, M.D.C. The role of Mo in the chemical composition and semiconductive behaviour of oxide films formed on stainless steels. *Corros. Sci.* **1999**, *41*, 17–34. [[CrossRef](#)]
6. Chen, Q.; Yan, Z.; Guo, L.; Zhang, H.; Zhang, L.; Kim, K.; Li, X.; Wang, W. Enhancing the acid orange dye degradation efficiency of Mg-based glassy alloys with introducing porous structure and zinc oxide. *J. Alloys Compd.* **2020**, *831*, 154817. [[CrossRef](#)]
7. Stokłosa, Z.; Rasek, J.; Kwapuliński, P.; Badura, G.; Haneczok, G.; Pająk, L.; Lelaćko, J.; Kolano-Burian, A. Magnetic, electrical and plastic properties of Fe₇₆Nb₂Si₁₃B₉, Fe₇₅Ag₁Nb₂Si₁₃B₉ and Fe₇₅Cu₁Nb₂Si₁₃B₉ amorphous alloys. *J. Alloys Compd.* **2011**, *509*, 9050–9054. [[CrossRef](#)]
8. Li, L.Y.; Sun, C.H.; Ruan, Y.; Wei, B. Duplex corrosion mechanisms correlated to α/γ phase selection in containerlessly processed Fe-Cr-Ni-Mo alloy. *Corros. Sci.* **2023**, *221*, 111311. [[CrossRef](#)]
9. Kobayashi, A.; Yano, S.; Kimura, H.; Inoue, A. Mechanical property of Fe-base metallic glass coating formed by gas tunnel type plasma spraying. *Surf. Coat. Technol.* **2008**, *202*, 2513–2518. [[CrossRef](#)]
10. Yoon, S.; Kim, J.; Bae, G.; Kim, B.; Lee, C. Formation of coating and tribological behavior of kinetic sprayed Fe-based bulk metallic glass. *J. Alloys Compd.* **2011**, *509*, 347–353. [[CrossRef](#)]
11. Zenebe, D.; Yi, S.; Kim, S.S. Sliding friction and wear behavior of Fe-based bulk metallic glass in 3.5% NaCl solution. *J. Mater. Sci.* **2011**, *47*, 1446–1451. [[CrossRef](#)]
12. Zhang, C.; Liu, L.; Chan, K.C.; Chen, Q.; Tang, C.Y. Wear behavior of HVOF-sprayed Fe-based amorphous coatings. *Intermetallics* **2012**, *29*, 80–85. [[CrossRef](#)]
13. Lekakh, S.N.; Buchely, M.; Li, M.; Godlewski, L. Effect of Cr and Ni concentrations on resilience of cast Nb-alloyed heat resistant austenitic steels at extreme high temperatures. *Mater. Sci. Eng. A* **2023**, *873*, 145027. [[CrossRef](#)]
14. Xiang, S.; Fan, Z.; Chen, T.; Lian, X.; Guo, Y. Microstructure evolution and creep behavior of nitrogen-bearing austenitic Fe–Cr–Ni heat-resistant alloys with various carbon contents. *J. Mater. Res. Technol.* **2023**, *23*, 316–330. [[CrossRef](#)]
15. Long, Z.L.; Chang, C.T.; Ding, Y.H.; Shao, Y.; Zhang, P.; Shen, B.L.; Inoue, A. Corrosion behavior of Fe-based ferromagnetic (Fe, Ni)–B–Si–Nb bulk glassy alloys in aqueous electrolytes. *J. Non-Cryst. Solids* **2008**, *354*, 4609–4613. [[CrossRef](#)]
16. Hashimoto, K. What we have learned from studies on chemical properties of amorphous alloys? *Appl. Surf. Sci.* **2011**, *257*, 8141–8150. [[CrossRef](#)]
17. Tsai, P.H.; Xiao, A.C.; Li, J.B.; Jang, J.S.C.; Chu, J.P.; Huang, J.C. Prominent Fe-based bulk amorphous steel alloy with large supercooled liquid region and superior corrosion resistance. *J. Alloys Compd.* **2014**, *586*, 94–98. [[CrossRef](#)]
18. Zohdi, H.; Shahverdi, H.R.; Hadavi, S.M.M. Effect of Nb addition on corrosion behavior of Fe-based metallic glasses in Ringer’s solution for biomedical applications. *Electrochem. Commun.* **2011**, *13*, 840–843. [[CrossRef](#)]
19. Ni, H.S.; Liu, X.H.; Chang, X.C.; Hou, W.L.; Liu, W.; Wang, J.Q. High performance amorphous steel coating prepared by HVOF thermal spraying. *J. Alloys Compd.* **2009**, *467*, 163–167. [[CrossRef](#)]
20. Otsubo, F.; Kishitake, K. Corrosion Resistance of Fe-16%Cr-30%Mo-(C,B,P) Amorphous Coatings Sprayed by HVOF and APS Processes. *Mater. Trans.* **2005**, *46*, 80–83. [[CrossRef](#)]
21. Garfias-Mesias, L.F.; Sykes, J.M.; Tuck, C.D.S. The effect of phase compositions on the pitting corrosion of 25 Cr duplex stainless steel in chloride solutions. *Corros. Sci.* **1996**, *38*, 1319–1330. [[CrossRef](#)]
22. Cleland, J.H. What does the pitting resistance equivalent really tell us? *Eng. Fail. Anal.* **1996**, *3*, 65–69. [[CrossRef](#)]
23. Liljas, M.; Johansson, P.; Liu, H.-P.; Olsson, C.-O.A. Development of a Lean Duplex Stainless Steel. *Steel Res. Int.* **2008**, *79*, 466–473. [[CrossRef](#)]
24. Tan, M.-W.; Akiyama, E.; Kawashima, A.; Asami, K.; Hashimoto, K. The effect of air exposure on the corrosion behavior of amorphous Fe-8Cr-Mo-13P-7C alloys in 1 M HCl. *Corros. Sci.* **1995**, *37*, 1289–1301. [[CrossRef](#)]
25. Jung, K.; Ahn, S.; Kim, Y.; Oh, S.; Ryu, W.-H.; Kwon, H. Alloy design employing high Cr concentrations for Mo-free stainless steels with enhanced corrosion resistance. *Corros. Sci.* **2018**, *140*, 61–72. [[CrossRef](#)]
26. Zhang, C.; Li, Q.; Xie, L.; Zhang, G.; Mu, B.; Chang, C.; Li, H.; Ma, X. Development of novel Fe-based bulk metallic glasses with excellent wear and corrosion resistance by adjusting the Cr and Mo contents. *Intermetallics* **2023**, *153*, 107801. [[CrossRef](#)]
27. Wang, Y.; Yu, H.; Wang, L.; Li, M.; Si, R.; Sun, D. Research on the structure-activity relationship of Fe-Cr alloy in marine environment based on synchrotron radiation: Effect of Cr content. *Surf. Interfaces* **2021**, *26*, 101370. [[CrossRef](#)]
28. Hua, Y.; Mohammed, S.; Barker, R.; Neville, A. Comparisons of corrosion behaviour for X65 and low Cr steels in high pressure CO₂-saturated brine. *J. Mater. Sci. Technol.* **2020**, *41*, 21–32. [[CrossRef](#)]
29. Yan, J.; Liu, T.; Wang, M.; Sun, J.; Dong, S.; Zhao, L.; Wang, Q. Constitutional supercooling and corresponding microstructure transition triggered by high magnetic field gradient during directional solidification of Al-Fe eutectic alloy. *Mater. Charact.* **2022**, *188*, 111920. [[CrossRef](#)]
30. Qi, Z.G.; Chen, Q.; Feng, Y.; Liu, H.Z.; Wang, Z.X.; Song, Z.Q.; Yan, Z.C.; Guo, L.Y.; Zhang, X.H.; Wang, W.M. Light activated methylene blue degradation by magnetic Fe₈₀P₂₀-(x = 0, 4, 7 and 13) glassy ribbons. *J. Alloys Compd.* **2023**, *953*, 170135. [[CrossRef](#)]

31. Meng, L.L.; Li, X.Y.; Pang, J.; Wang, L.; An, B.; Yin, L.J.; Song, K.K.; Wang, W.M. Casting Atmosphere Effects on the Precipitates, Magnetism, and Corrosion Resistance of Fe78Si9B13 Glassy Alloys. *Metall. Mater. Trans. A* **2013**, *44*, 5122–5133. [[CrossRef](#)]
32. Ma, J.; Zhang, B.; Fu, Y.; Hu, X.; Cao, X.; Pan, Z.; Wei, Y.; Luo, H.; Li, X. Effect of cold deformation on corrosion behavior of selective laser melted 316L stainless steel bipolar plates in a simulated environment for proton exchange membrane fuel cells. *Corros. Sci.* **2022**, *201*, 110257. [[CrossRef](#)]
33. Lu, K.; Sui, M.L.; Wang, J.T. Eutectic crystallization products and their orientation relationship in amorphous TM-M alloys. *J. Mater. Sci. Lett.* **1990**, 630–632. [[CrossRef](#)]
34. Lu, Z.P.; Liu, C.T. A new glass-forming ability criterion for bulk metallic glasses. *Acta Mater.* **2002**, *50*, 3501–3512. [[CrossRef](#)]
35. Han, B.; Chen, Y.; Tao, W.; Lei, Z.; Li, H.; Guo, S.; Li, P. Nano-indentation investigation on the local softening of equiaxed zone in 2060-T8/2099-T83 aluminum-lithium alloys T-joints welded by double-sided laser beam welding. *J. Alloys Compd.* **2018**, *756*, 145–162. [[CrossRef](#)]
36. Hatada, R.; Flege, S.; Ashraf, M.N.; Timmermann, A.; Schmid, C.; Ensinger, W. The Influence of Preparation Conditions on the Structural Properties and Hardness of Diamond-Like Carbon Films, Prepared by Plasma Source Ion Implantation. *Coatings* **2020**, *10*, 360. [[CrossRef](#)]
37. Jiang, B.; Doi, K.; Tsuchiya, K.; Kawano, Y.; Kori, A.; Ikushima, K. Micromechanical properties of steel corrosion products in concrete studied by nano-indentation technique. *Corros. Sci.* **2020**, *163*, 108304. [[CrossRef](#)]
38. Amin, M.A.; Abd El Rehim, S.S.; Abdel-Fatah, H.T.M. Electrochemical frequency modulation and inductively coupled plasma atomic emission spectroscopy methods for monitoring corrosion rates and inhibition of low alloy steel corrosion in HCl solutions and a test for validity of the Tafel extrapolation method. *Corros. Sci.* **2009**, *51*, 882–894. [[CrossRef](#)]
39. Amin, M.A.; Khaled, K.F.; Fadl-Allah, S.A. Testing validity of the Tafel extrapolation method for monitoring corrosion of cold rolled steel in HCl solutions – Experimental and theoretical studies. *Corros. Sci.* **2010**, *52*, 140–151. [[CrossRef](#)]
40. Zhang, S.D.; Zhang, W.L.; Wang, S.G.; Gu, X.J.; Wang, J.Q. Characterisation of three-dimensional porosity in an Fe-based amorphous coating and its correlation with corrosion behaviour. *Corros. Sci.* **2015**, *93*, 211–221. [[CrossRef](#)]
41. Chong, K.; Gao, Y.; Zhang, Z.; Zou, Y.; Liang, X. Thermal stability and corrosion behavior of a novel Zr_{22.5}Ti_{22.5}Hf_{22.5}Ni_{22.5}Ta₁₀ high-entropy amorphous alloy. *Corros. Sci.* **2023**, *213*, 110979. [[CrossRef](#)]
42. Berger, J.E.; Jorge, A.M.; Koga, G.Y.; Roche, V.; Kiminami, C.S.; Bolfarini, C.; Botta, W.J. Influence of chromium concentration and partial crystallization on the corrosion resistance of FeCrNiB amorphous alloys. *Mater. Charact.* **2021**, *179*, 111369. [[CrossRef](#)]
43. Botta, W.J.; Berger, J.E.; Kiminami, C.S.; Roche, V.; Nogueira, R.P.; Bolfarini, C. Corrosion resistance of Fe-based amorphous alloys. *J. Alloys Compd.* **2014**, *586*, S105–S110. [[CrossRef](#)]
44. Coimbra, D.D.; Zepon, G.; Koga, G.Y.; Godoy Pérez, D.A.; Paes de Almeida, F.H.; Roche, V.; Lepretre, J.C.; Jorge, A.M.; Kiminami, C.S.; Bolfarini, C.; et al. Corrosion properties of amorphous, partially, and fully crystallized Fe₆₈Cr₈Mo₄Nb₄B₁₆ alloy. *J. Alloys Compd.* **2020**, *826*, 154123. [[CrossRef](#)]
45. Fan, Y.; Zhang, S.; Xu, X.; Miao, J.; Zhang, W.; Wang, T.; Chen, C.; Wei, R.; Li, F. Effect of the substitution of Si for B on thermal stability, magnetic properties and corrosion resistance in novel Fe-rich amorphous soft magnetic alloy. *Intermetallics* **2021**, *138*, 107306. [[CrossRef](#)]
46. Han, Y.; Chang, C.T.; Zhu, S.L.; Inoue, A.; Louzguine-Luzgin, D.V.; Shalaan, E.; Al-Marzouki, F. Fe-based soft magnetic amorphous alloys with high saturation magnetization above 1.5 T and high corrosion resistance. *Intermetallics* **2014**, *54*, 169–175. [[CrossRef](#)]
47. Han, Y.; Kong, F.L.; Han, F.F.; Inoue, A.; Zhu, S.L.; Shalaan, E.; Al-Marzouki, F. New Fe-based soft magnetic amorphous alloys with high saturation magnetization and good corrosion resistance for dust core application. *Intermetallics* **2016**, *76*, 18–25. [[CrossRef](#)]
48. Koga, G.Y.; Nogueira, R.P.; Roche, V.; Yavari, A.R.; Melle, A.K.; Gallego, J.; Bolfarini, C.; Kiminami, C.S.; Botta, W.J. Corrosion properties of Fe–Cr–Nb–B amorphous alloys and coatings. *Surf. Coat. Technol.* **2014**, *254*, 238–243. [[CrossRef](#)]
49. Liu, Y.; Li, J.; Sun, Y.; He, A.; Dong, Y.; Wang, Y. Effect of annealing temperature on magnetic properties and corrosion resistance of Fe_{75.8}Si₁₂B₈Nb_{2.6}Cu_{0.6}P₁ alloy. *J. Mater. Res. Technol.* **2021**, *15*, 3880–3894. [[CrossRef](#)]
50. Meghwal, A.; Pinches, S.; King, H.J.; Schulz, C.; Stanford, N.; Hall, C.; Berndt, C.C.; Ang, A.S.M. Fe-based amorphous coating for high-temperature wear, marine and low pH environments. *Materialia* **2022**, *25*, 101549. [[CrossRef](#)]
51. Sunbul, S.E.; Akyol, S.; Onal, S.; Ozturk, S.; Sozeri, H.; Icin, K. Effect of Co, Cu, and Mo alloying metals on electrochemical and magnetic properties of Fe-B alloy. *J. Alloys Compd.* **2023**, *947*, 169652. [[CrossRef](#)]
52. Vasić, M.M.; Simatović, I.S.; Radović, L.; Minić, D.M. Influence of microstructure of composite amorphous/nanocrystalline Fe₇₂Ni₈Si₁₀B₁₀ alloy on the corrosion behavior in various environments. *Corros. Sci.* **2022**, *204*, 110403. [[CrossRef](#)]
53. Wu, L.; Zhou, Z.; Zhang, K.; Zhang, X.; Wang, G. Electrochemical and passive film evaluation on the corrosion resistance variation of Fe-based amorphous coating affected by high temperature. *J. Non-Cryst. Solids* **2022**, *597*, 121892. [[CrossRef](#)]
54. Wang, P.; Qi, W.; Yang, K.; Qiao, Y.; Wang, X.; Zheng, T.; Bai, C.; Liu, Z.; Zhang, X. Systematic investigation of the oxidation behavior of Fe-Cr-Al cladding alloys in high-temperature steam. *Corros. Sci.* **2022**, *207*, 110595. [[CrossRef](#)]
55. Qin, C.; Hu, Q.; Li, Y.; Wang, Z.; Zhao, W.; Louzguine-Luzgin, D.V.; Inoue, A. Novel bioactive Fe-based metallic glasses with excellent apatite-forming ability. *Mater. Sci. Eng. C* **2016**, *69*, 513–521. [[CrossRef](#)]
56. Wu, G.; Tan, X.; Li, G.; Hu, C. Effect of preparation method on the physical and catalytic property of nanocrystalline Fe₂O₃. *J. Alloys Compd.* **2010**, *504*, 371–376. [[CrossRef](#)]
57. Tian, W.-P.; Yang, H.-W.; Zhang, S.-D. Synergistic Effect of Mo, W, Mn and Cr on the Passivation Behavior of a Fe-Based Amorphous Alloy Coating. *Acta Metall. Sin. (Engl. Lett.)* **2017**, *31*, 308–320. [[CrossRef](#)]

58. Wang, Y.; Jiang, S.L.; Zheng, Y.G.; Ke, W.; Sun, W.H.; Wang, J.Q. Electrochemical behaviour of Fe-based metallic glasses in acidic and neutral solutions. *Corros. Sci.* **2012**, *63*, 159–173. [[CrossRef](#)]
59. Wu, J.; Zhang, S.D.; Sun, W.H.; Gao, Y.; Wang, J.Q. Enhanced corrosion resistance in Fe-based amorphous coatings through eliminating Cr-depleted zones. *Corros. Sci.* **2018**, *136*, 161–173. [[CrossRef](#)]
60. Xu, D.D.; Zhou, B.L.; Wang, Q.Q.; Zhou, J.; Yang, W.M.; Yuan, C.C.; Xue, L.; Fan, X.D.; Ma, L.Q.; Shen, B.L. Effects of Cr addition on thermal stability, soft magnetic properties and corrosion resistance of FeSiB amorphous alloys. *Corros. Sci.* **2018**, *138*, 20–27. [[CrossRef](#)]
61. Zhai, H.; Yuan, H.; Li, W.; Zhang, X.; Li, X.; Cai, A. Corrosion resistance mechanisms of detonation sprayed Fe-based amorphous coating on AZ31B magnesium alloy. *J. Non-Cryst. Solids* **2022**, *576*, 121276. [[CrossRef](#)]
62. Čekerevac, M.; Simičić, M.; Bujanović, L.N.; Popović, N. The influence of silicate and sulphate anions on the anodic corrosion and the transpassivity of iron and silicon-rich steel in concentrated KOH solution. *Corros. Sci.* **2012**, *64*, 204–212. [[CrossRef](#)]
63. Luo, H.; Su, H.; Dong, C.; Li, X. Passivation and electrochemical behavior of 316L stainless steel in chlorinated simulated concrete pore solution. *Appl. Surf. Sci.* **2017**, *400*, 38–48. [[CrossRef](#)]
64. Zhang, Y.; Song, B.; Ming, J.; Yan, Q.; Wang, M.; Cai, C.; Zhang, C.; Shi, Y. Corrosion mechanism of amorphous alloy strengthened stainless steel composite fabricated by selective laser melting. *Corros. Sci.* **2020**, *163*, 108241. [[CrossRef](#)]
65. Kroll, R.; Kearns, P.; Usman, B.J.; Zhou, X.; Engelberg, D.L. A novel approach to determine cathodic passivation characteristics and semiconducting properties of pure aluminium 99.5 wt% and aluminium alloy 7075-T6 with an electrochemical pen electrode. *Corros. Sci.* **2023**, *211*, 110898. [[CrossRef](#)]
66. Liu, M.; Cheng, X.; Li, X.; Pan, Y.; Li, J. Effect of Cr on the passive film formation mechanism of steel rebar in saturated calcium hydroxide solution. *Appl. Surf. Sci.* **2016**, *389*, 1182–1191. [[CrossRef](#)]
67. Shi, J.; Ming, J.; Wu, M. Electrochemical behavior and corrosion products of Cr-modified reinforcing steels in saturated Ca(OH)₂ solution with chlorides. *Cem. Concr. Compos.* **2020**, *110*, 103587. [[CrossRef](#)]
68. Song, G.; Atrens, A.; John, D.S.; Wu, X.; Nairn, J. The anodic dissolution of magnesium in chloride and sulphate solutions. *Corros. Sci.* **1997**, *39*, 1981–2004. [[CrossRef](#)]
69. Lamaka, S.V.; Shchukin, D.G.; Andreeva, D.V.; Zheludkevich, M.L.; Möhwald, H.; Ferreira, M.G.S. Sol-Gel/Polyelectrolyte Active Corrosion Protection System. *Adv. Funct. Mater.* **2008**, *18*, 3137–3147. [[CrossRef](#)]
70. Song, G.-L.; Unocic, K.A. The anodic surface film and hydrogen evolution on Mg. *Corros. Sci.* **2015**, *98*, 758–765. [[CrossRef](#)]
71. Xu, J.; Liu, L.; Li, Z.; Munroe, P.; Xie, Z.H. Niobium addition enhancing the corrosion resistance of nanocrystalline Ti₅Si₃ coating in H₂SO₄ solution. *Acta Mater.* **2014**, *63*, 245–260. [[CrossRef](#)]

Disclaimer/Publisher’s Note: The statements, opinions and data contained in all publications are solely those of the individual author(s) and contributor(s) and not of MDPI and/or the editor(s). MDPI and/or the editor(s) disclaim responsibility for any injury to people or property resulting from any ideas, methods, instructions or products referred to in the content.